9

X-ray Diffuse Scattering Near Bragg Reflections for the Study of Clustered Defects in Crystalline Materials

Bennett C. Larson

Materials Science and Technology Division, Oak Ridge National Laboratory, Oak Ridge, TN 37831, USA

Abstract

The fundamental aspects of diffuse scattering from lattice defects within the coherent wave theory are reviewed, and the use of Huang and asymptotic diffuse scattering for the determination of the size, type, and internal structure of clustered defects is discussed. The scattering amplitude for diffuse scattering from lattice defects is presented within the single defect approximation, and the physical interpretation of the asymptotic diffuse scattering from dislocation loops and precipitates is discussed in terms of local Bragg scattering. The importance of using detailed and accurate displacement fields for calculating diffuse scattering cross sections for dislocation loops and coherent precipitates is emphasized, and examples of the measurement of size distributions for vacancy and interstitial loops and for coherent precipitates in Cu are revisited. In addition, the use of submicrometer-diameter X-ray microbeams to perform depth-resolved diffuse scattering measurements of vacancy and interstitial loop distributions in 10 MeV self-ion-implanted silicon single crystals is discussed.

1 Introduction

The analysis of diffuse scattering near Bragg reflections represents a powerful method for the study of defect clusters that induce lattice distortions in crystalline materials. Krivoglaz, Dederichs, and Trinkaus [1–6] were instrumental in analyzing the form and intensity of the Huang diffuse scattering resulting from the long-range elastic distortion fields surrounding point defects and defect clusters.

imo-barabash-09.indd 139 2/13/09 8:00:17 AM

Their work further considered the scattering in the so-called asymptotic scattering region (beyond the Huang scattering region) that is characterized by local Bragg scattering from the relatively large distortions near defect clusters [5,7,8]. Although the asymptotic diffuse scattering associated with the large lattice displacements near defect clusters cannot be fully specified in closed form, the physical interpretation of asymptotic diffuse scattering in terms of particle size- and strain gradient-broadened Bragg-like scattering from locally rotated or dilatated regions near defect clusters is clear. Fortunately, accurate diffuse scattering cross sections can be obtained for this region through numerical integration of lattice sums and the use of numerically calculated elastic displacement fields for dislocation loops and precipitates [8–12].

The ability to calculate accurate diffuse scattering cross sections for defect clusters has been key for using diffuse scattering as a quantitative tool to investigate defect clusters in crystals [8–11]. X-ray diffuse scattering has been used in a large number of studies of irradiation-induced and intrinsic defect clusters in crystals, as discussed in original papers and reviews [13–27]. Thermodynamic precipitation of coherent second-phase particles is of both fundamental and technological importance for advanced materials. Alloy precipitation and both electron and neutron irradiations produce defects distributed uniformly throughout bulk samples. However, ion irradiations typically involve penetration depths of only a few microns below surfaces, and because ion damage is strongly energy dependent, they produce defect distributions that are strongly depth dependent. Understanding the generation and annealing characteristics of ion irradiation-induced defects is important for simulating high-dose neutron irradiation damage, and ion damage has become increasingly important in relation to ion implantation processing steps incorporated into electronic device manufacture.

In this chapter, we discuss the fundamental concepts of diffuse scattering, the information available on defect clusters from diffuse scattering near Bragg reflections, and the application of submicron spatial resolution X-ray microbeams for depth-resolved studies of ion implantation-induced defects in silicon. The results of depth-dependent differential diffuse scattering measurements, made in cross sections on self-ion-irradiated silicon, are presented in terms of size distributions and point defect concentrations for vacancy and interstitial loops, and the relative merits of cross section and plan-view diffuse scattering techniques are discussed.

2 Diffuse Scattering and Coherent Wave-Scattering Theory

X-ray scattering from lattice defects is generally quite weak; therefore, the cross section for scattering of an incoming plane wave $e^{i\mathbf{k}_o\cdot\mathbf{r}}$ with wave vector $\mathbf{k_o}$ into an outgoing wave $e^{i\mathbf{k}\cdot\mathbf{r}}$ with wave vector $\mathbf{k}$ is usually written in terms of the kinematic or first Born approximation with no provision for multiple scattering. In the first Born approximation, the differential cross section for an ensemble of atoms is given by

$$\frac{d\sigma(\mathbf{K})}{d\Omega} = \left|V(\mathbf{K})\right|^2, \tag{9.1}$$

where $\mathbf{K}=\mathbf{k}-\mathbf{k_o}$ and $V(\mathbf{K})$ is the Fourier transform of the scattering potential $V(\mathbf{r}) = \sum_i r_e f_i(\mathbf{K})\delta(\mathbf{r}-\mathbf{r}_i)$.

The atomic scattering length for X-rays, $r_e f_i(\mathbf{K})$, is given by the product of the classical electron

radius, r_e, and the atomic form factor $f_i(\mathbf{K})$. The lattice sites are specified by $\mathbf{r}_i = \mathbf{r}_i^o + \mathbf{s}_i$, in which $\mathbf{r}_i^o$ represents the undistorted lattice site and $\mathbf{s}_i \equiv \mathbf{s}(\mathbf{r}_i)$ specifies the displacement from the ith periodic lattice site. The scattering amplitude is then defined by

$$\frac{d\sigma(\mathbf{K})}{d\Omega} = \left| r_e f(\mathbf{K}) \right|^2 \left| A(\mathbf{K}) \right|^2 = \left| \sum_i r_e f_i(\mathbf{K}) e^{i\mathbf{K}\cdot\mathbf{r}_i} \right|^2 . \tag{9.2}$$

This is the total elastic scattering cross section for the sample and so contains Bragg reflections for average periodic $\mathbf{r}_i$ expanded by image forces and diffuse scattering components generated by deviations $\mathbf{s}(\mathbf{r}_i)$ from periodic lattice sites (e.g., by phonons, point defects, clusters of point defects, second-phase precipitates, or dislocations) [1,3,17]. As pointed out by Krivoglaz [1], line defects such as dislocations are a special case in that they are not localized defects and their slowly decaying strain field falls off only as $1/r$. Therefore, the static Debye-Waller factor diverges for crystals with dislocations as a signature of the destruction of long-range periodicity. The remaining strain-broadened and particle-size-broadened scattering may be strongly peaked, but according to the strict definition of Bragg scattering from long-range periodic structures, it represents diffuse scattering that is often referred to as local Bragg-like or Stokes-Wilson scattering within the deformation microstructure [28]. Although dislocation loops will be addressed here in terms of point-defect clusters in otherwise long-range periodic crystals, diffuse scattering from dislocation lines and tangles is fundamentally different in origin from that of point defects, dislocation loops, and clusters and will not be considered here.

The distinction between sharply peaked (coherent) Bragg scattering and the more smoothly varying (incoherent) diffuse scattering is not easily defined within the kinematical first Born approximation theory discussed above because Huang scattering from both thermal vibrations and lattice defects diverges at Bragg reflections. On the other hand, the scattering processes are, in fact, well defined quantum-mechanically in terms of changes of any quantum number in the state of the sample, and, accordingly, the separation is well defined within the formal theory of scattering, which inherently includes multiple scattering. As discussed by Lax [29] and in more detail by Dederichs [5,17], the separation of the Bragg (coherent) scattering from the diffuse (incoherent) scattering for crystalline samples containing localized defects is well defined in terms of the so-called coherent wave theory, which is based on the formally exact Lippman-Schwinger equation [17]. Although a rigorous and complete presentation of the coherent wave analysis is outside the scope of this chapter, it is instructive to recall the elegant arguments of the coherent wave theory that led intuitively to the so-called single-defect approximation, which forms the underlying basis of diffuse scattering investigations of statistically distributed lattice defects.

In outlining the coherent wave approach, we follow Lax [29] and Dederichs [2,17] and consider a periodic assembly of atoms with a statistical distribution of point defects or point-defect clusters that generate frozen-in displacements by their elastic distortion fields. The separation between Bragg and diffuse scattering within the coherent wave formalism is identified by performing a formal (theoretical) interference experiment to determine what part of the scattered wave remains quantum-mechanically coherent within the scattering process and hence is able to interfere with the incoming wave. Defining ψ to be the solution to the scattering of an incoming wave, ϕ, by a particular statistical distribution of defects within the sample, the intensity (density) of scattered radiation is given by $\psi^* \psi = |\psi|^2$. The

experimentally observed scattering from a statistically random distribution of defects is given by averaging $|\psi|^2$ over all possible lattice defect configurations. Denoting this statistical average by $\langle\ \rangle$, the measured intensity is then given by $\langle|\psi|^2\rangle$.

The formal interference experiment to determine what part of ψ remains coherent with the incident beam and which part represents diffuse scattering is defined by

$$\langle|\phi+\psi|^2\rangle = \langle\phi^*\phi+\phi^*\psi+\psi^*\phi+\psi^*\psi\rangle, \tag{9.3}$$

which, after performing the implied statistical averages and adding and subtracting $\langle\psi^*\rangle\langle\psi\rangle$, leads to the important result that

$$\langle|\phi+\psi|^2\rangle = |\phi+\langle\psi\rangle|^2 + \langle|\psi|^2\rangle - |\langle\psi\rangle|^2 . \tag{9.4}$$

Equation 9.4 indicates that only $\langle\psi\rangle$ remains absolutely coherent with ϕ and that the remaining fraction $\langle|\psi|^2\rangle - |\langle\psi\rangle|^2$ is incoherent or, according to Lax [29], only relatively (i.e., not absolutely) coherent with the incoming beam ϕ. We note that the symbolic form of the incoherent term $\langle|\psi|^2\rangle - |\langle\psi\rangle|^2$ is just the form that is associated with fluctuation scattering (or departures from mean field behavior). It is natural then to associate the coherent term with the Bragg scattering term, where $\langle\psi\rangle$ indicates that the Bragg scattering that remains coherent is reduced by a Debye-Waller factor (as will be seen below) that is introduced by the averaging over statistically distributed defect distributions. Equation 9.4 then leads to the following intuitive separation of the diffuse scattering (or fluctuation scattering) cross section from the total scattering cross section by subtracting the Bragg scattering:

$$\left[\frac{d\sigma(\mathbf{K})}{d\Omega}\right]_{Diffuse} = \left[\frac{d\sigma(\mathbf{K})}{d\Omega}\right]_{Total} - \left[\frac{d\sigma(\mathbf{K})}{d\Omega}\right]_{Bragg} \tag{9.5}$$

Equation 9.4 assures this to be rigorously true in a quantum-mechanical sense and not simply by an empirically derived result. As will be mentioned later, however, separating coherent scattering, inelastic (Compton) scattering, and thermal diffuse scattering from defect diffuse scattering is not at all a simple or straightforward task experimentally, even though it is well defined theoretically.

Now, if one associates ψ with $\sum_i r_e f_i e^{i\mathbf{K}\cdot\mathbf{r}_i}$ and understands $f_i = f_i(\mathbf{K})$ for shorthand, the following expressions are obtained for the diffuse scattering components:

$$\langle|\psi|^2\rangle = \left\langle\left|\sum_i r_e f_i e^{i\mathbf{K}\cdot\mathbf{r}_i}\right|^2\right\rangle = \left\langle\sum_{i,j} r_e^2 f_i f_j e^{i\mathbf{K}\cdot(\mathbf{r}_i-\mathbf{r}_j)}\right\rangle, \tag{9.6}$$

$$\left|\langle\psi\rangle\right|^2 = \left|\left\langle \sum_i r_e f_i e^{i\mathbf{K}\bullet\mathbf{r}_i} \right\rangle\right|^2 = \left\langle \sum_i r_e f_i e^{i\mathbf{K}\bullet\mathbf{r}_i} \right\rangle \left\langle \sum_j r_e f_j e^{-i\mathbf{K}\bullet\mathbf{r}_j} \right\rangle . \tag{9.7}$$

If we further write **K = H + q**, where **H** is a reciprocal lattice vector and **q** is a vector within the Brillouin zone, and recall that $\mathbf{r}_i = \mathbf{r}_i^o + \mathbf{s}_i$, we obtain with $\mathbf{H}\bullet\mathbf{r}_i^o = 2\pi n$,

$$\left[\frac{d\sigma(\mathbf{K})}{d\Omega}\right]_{Diffuse} = \sum_{i,j} r_e^2 f_i f_j e^{i\mathbf{q}\bullet(\mathbf{r}_i^o - \mathbf{r}_j^o)} \left[\left\langle e^{i\mathbf{K}\bullet(\mathbf{s}_i - \mathbf{s}_j)} \right\rangle - \left\langle e^{i\mathbf{K}\bullet\mathbf{s}_i} \right\rangle \left\langle e^{-i\mathbf{K}\bullet\mathbf{s}_j} \right\rangle\right] . \tag{9.8}$$

Following Dederichs [2,3,17], after detailed consideration of overlapping defect displacement fields for statistically random defect sites and the implications of image forces, which implies that $\mathbf{r}_i$ now refers to the average expanded (or contracted) lattice positions, Equation 9.8 yields

$$\left[\frac{d\sigma(\mathbf{K})}{d\Omega}\right]_{Diffuse} = \left|\sum_i r_e f_i e^{-L(\mathbf{K})} e^{i\mathbf{q}\bullet\mathbf{r}_i} \left[e^{i\mathbf{K}\bullet\mathbf{s}(\mathbf{r}_i)} - 1\right]\right|^2 . \tag{9.9}$$

Including the scattering from the defect atoms located at position $\mathbf{r}_j^d$ (with respect to average lattice positions) generating the displacements $\mathbf{s}(\mathbf{r}_i)$, Equation 9.9 becomes

$$\left[\frac{d\sigma(\mathbf{K})}{d\Omega}\right]_{Diffuse} = \left|\sum_j^{n^d} r_e f_j^d e^{i\mathbf{H}\bullet\mathbf{r}_j^d} e^{i\mathbf{q}\bullet\mathbf{r}_j^d} + \sum_i r_e f_i e^{-L(\mathbf{K})} e^{i\mathbf{q}\bullet\mathbf{r}_i} \left[e^{i\mathbf{K}\bullet\mathbf{s}(\mathbf{r}_i)} - 1\right]\right|^2 , \tag{9.10}$$

where n^d is the number of atoms in the defect/cluster and L(**K**) is the static Debye-Waller factor given by $L(\mathbf{K}) = c\sum_i [1 - \cos(\mathbf{K}\bullet\mathbf{s}(\mathbf{r}_i)]$, with c representing the fractional concentration of defects (i.e., defects per atom) within the lattice.

Equation 9.10 corresponds to the so-called single-defect approximation for randomly distributed defects, where the first term represents the direct or Laue scattering from the atoms in the defect cluster (i.e., dislocation loop, coherent precipitate, or loose aggregate) and the second term represents the scattering from the surrounding atoms that are displaced $\mathbf{s}(\mathbf{r}_i)$ from their regular lattice positions by the elastic distortion field surrounding the defect clusters.

As discussed above, the single-defect approximation refers to the specific case of a statistically large number of defects that are randomly distributed within an otherwise undistorted periodic crystal. The simplicity of the formula and the ability to consider only the distortion field for a single defect in the calculation of the cross section are due to the fact that the cross-terms in the scattering between individual defects cancel identically for randomly distributed defect sites. It should be emphasized also that the scattering formalism specifically assumes that the displacement fields of all defects overlap completely since their displacements fall off as $1/r^2$ with no cutoff. Hence each defect impacts the positions of atoms in every part of the sample, and the forces at the edges of the sample lead to the expansion/contraction of the average periodic lattice. Implicit in the process is the assumption that the density and strength of the defects are low enough that they do not distort the crystal lattice so much as to preclude the notion of an average periodic lattice, which implies that within a dynamical diffraction extinction distance for the periodic average lattice there is a statistically random distribution of defects.

3 Evaluation of Diffuse Scattering Cross Sections for Small *q* and Large *q*

In order to understand and interpret diffuse scattering from lattice defects, methods to perform the lattice sums involved in the cross sections in Equation 9.10 have been the focus of considerable attention for more than half a century, both in closed form and numerically [1–8,10–12,20]. The direct (or Laue) scattering term in the amplitude is a rather straightforward Fourier transform of the atoms comprising the defects themselves, and so presents little difficulty [5,11]. The scattering amplitude associated with the distortion of the surrounding crystal (the second term in Equation 9.10) is more complex, however, and requires a combination of analytic and numerical tools for evaluation. For small $\mathbf{q}$, the exponential inside the bracket in the distortion scattering function

$$\sum_i e^{i\mathbf{q}\bullet\mathbf{r}_i}\left[e^{i\mathbf{K}\bullet\mathbf{s}(\mathbf{r}_i)}-1\right] \tag{9.11}$$

can be expanded to obtain the so-called Huang scattering amplitude,

$$A_H(\mathbf{K}) = i\mathbf{K}\bullet\mathbf{s}(\mathbf{q}), \tag{9.12}$$

which can be evaluated analytically even for elastically anisotropic materials [3,5,11] and produces the well-known $1/q^2$ dependence of the Huang scattering intensity close to Bragg reflections. The ability to evaluate this leading term analytically is critical for both large and small q because the Huang amplitude is sensitive to the long-range elastic distortions and so converges very slowly in r. By removing the leading term from the sum and evaluating it analytically, the remaining portion of Equation 9.11 is given by

$$\sum_i e^{i\mathbf{q}\bullet\mathbf{r}_i}\left[e^{i\mathbf{K}\bullet\mathbf{s}(\mathbf{r}_i)}-1\right] \equiv i\mathbf{K}\bullet\mathbf{s}(\mathbf{q}) + \sum_i e^{i\mathbf{q}\bullet\mathbf{r}_i}\left[e^{i\mathbf{K}\bullet\mathbf{s}(\mathbf{r}_i)}-1-i\mathbf{K}\bullet\mathbf{s}(\mathbf{r}_i)\right], \tag{9.13}$$

which in sine and cosine notation is given by

$$\sum_i e^{i\mathbf{q}\bullet\mathbf{r}_i}\left[e^{i\mathbf{K}\bullet\mathbf{s}(\mathbf{r}_i)}-1\right] \equiv i\mathbf{K}\bullet\mathbf{s}(\mathbf{q}) + \sum_i e^{i\mathbf{q}\bullet\mathbf{r}_i}\left[\cos\left(\mathbf{K}\bullet\mathbf{s}(\mathbf{r}_i)\right)-1+i\sin\left(\mathbf{K}\bullet\mathbf{s}(\mathbf{r}_i)\right)-i\mathbf{K}\bullet\mathbf{s}(\mathbf{r}_i)\right]. \tag{9.14}$$

This form indicates immediately that only terms of order $\left(\mathbf{K}\bullet\mathbf{s}(\mathbf{r}_i)\right)^2$ and higher remain in the summation. Therefore, after subtracting the Huang amplitude from the summation and evaluating it analytically utilizing double-force tensors and Fourier-transformed elastic Greens functions [5], the second term falls off as $1/r^4$ or faster ($\mathbf{s}(\mathbf{r})\sim 1/r^2$) so that volume integrals converge as $1/r^2$ and so can be integrated without difficulty using numerically calculated displacement fields $\mathbf{s}(\mathbf{r})$ as discussed below.

The Huang scattering amplitude, given in closed form by Equation 9.12, is of course very strong for small q due to the fact that the amplitude diverges as $1/q$ [2,6,11]. The high intensity and the ability to specify accurately the angular dependence of the Huang scattering for both point defects and point defect clusters (loops, precipitates) makes the Huang scattering component attractive for investigating the local symmetry of lattice defects. However, Huang scattering information is, in practice, most powerful for point defects or very small clusters [2–6,16,30], where direct imaging techniques such as transmission electron microscopy (TEM) are not applicable. This is because the Huang scattering

amplitude does not provide direct information on cluster sizes except through the often-used (but actually rather crude [1,11,18]) approximation of $R \sim 1/q_c$ (or $R \sim 1/\left(\sqrt{Hb}q_c\right)$), where b is the Burgers vector for dislocation loops and q_c corresponds to the crossover from the Huang scattering $1/q^2$ dependence to the asymptotic scattering $1/q^4$ falloff for larger q. Even then the determination is heavily weighted toward larger sizes in distributions—the fourth power of the radius for loops and the sixth power of the radius for precipitates. Moreover, because of the square of the amplitude, it does not provide direct information on the vacancy versus interstitial nature of loops when both types are present.

For clustered defects such as dislocation loops or precipitates, Huang scattering measurements provide symmetry information [3,18], but if combinations of loops and precipitates or other types of structural deformation are present, symmetry information on individual types of defect clusters is not available. For sizes above $R \sim 10$ Å, TEM measurements are, of course, able to provide detailed information on defect cluster symmetry, morphology, and size for deformed and polycrystalline samples as well as for samples containing a mixture of defect types. On the other hand, when both vacancy and interstitial loops are present (such as in neutron-, electron-, or ion-irradiated materials), obtaining size distributions for each type of loop separately from TEM measurements becomes a very tedious process [14,15]. Moreover, when defect clusters are too small to be imaged definitively by TEM or for investigations such as cluster nucleation and sequential thermal growth studies, where nondestructive measurements are desired, X-ray diffuse scattering in the so-called asymptotic (large q) region beyond the Huang scattering region provides critical information not available by TEM [7,14].

Although scattering cross sections cannot be calculated in closed form for the large q asymptotic scattering regime, accurate numerical calculations can be made using Equation 9.13 [2,7,8,10,11,14,32]. As discussed originally by Stokes and Wilson in connection with straight dislocation distributions [28] and as shown for clustered defects by Trinkaus [5,7,8] within the infinitesimal distortion center approximation (i.e., assuming lattice displacements increase as $\sim 1/r^2$ down to zero r), diffuse scattering from the strongly deformed volumes close to defect clusters can be characterized as Bragg-like scattering from locally dilatated and rotated regions. Detailed cross section calculations using Equation 9.13 for both dislocation loops and coherent precipitates have verified the local Bragg scattering interpretation [8,10,11]. However, the numerical calculations further showed that it is critically important to use the actual deformation fields near dislocation loops and inside precipitates rather than to assume a $\sim 1/\hat{r}^2$ dependence for all r. This is because not only do the actual distortion fields depart markedly from $1/r^2$ for r less than the radius R but also the form of the actual displacement fields yield constant or nearly constant lattice parameters for $r < R$, which in turn introduces strong distortions in the $1/q^4$ dependence predicted by the infinitesimal distortion center approximation [5,7–11].

Accordingly, it is imperative to use accurate (numerically calculated) scattering cross sections based on actual defect cluster displacement fields for quantitative diffuse scattering investigations of defect cluster concentrations, sizes, and size distributions. As discussed in detail in the next section, the strong intensity distortions in the $1/q^4$ dependence are very informative; in fact, they provide direct size information for both dislocation loops and precipitate particles, and they also make it possible to extract separate size distributions for interstitial and vacancy loops. Moreover, the information on cluster size obtained from scattering derived from lattice positions $r < R$ is far more detailed and far more accurate than information on sizes determined using the above discussed transition from the Huang scattering ($1/q^2$) to the asymptotic scattering ($1/q^4$ or faster) regime.

As mentioned following Equation 9.5, the separation of Bragg scattering, electronic inelastic (i.e., Compton) scattering, and quasielastic thermal diffuse scattering from defect diffuse scattering experimentally is in reality a rather subjective process and, if not carried out properly, can have profound effects on the smallest q and largest q forms of the measured defect diffuse scattering patterns. At small q (close to the Bragg reflection) the defect diffuse scattering is overwhelmed by thermal diffuse scattering and by the Bragg tails, and at large q the defect cluster diffuse scattering is again dominated by thermal diffuse scattering and Compton inelastic scattering as the defect diffuse scattering falls off as $1/q^4$ or faster. For irradiation-induced defect clusters, it is possible to perform detailed measurements before the irradiation in most cases, and for precipitation from alloys, it is possible to perform such measurements before and after the precipitation process. However, for samples with intrinsic defect clusters in which the sample does not exist without the clusters, the background subtraction must be done with care, and in general, measurements at very small q and very large q should not be allowed to dominate the analyzed results in terms of very large clusters or very small defect clusters, respectively.

4 Asymptotic Diffuse Scattering

The distortion fields surrounding coherent precipitates and prismatic dislocation loops are depicted schematically in Figure 9.1. The illustrative lattice models in the Figure depict the distorted regions surrounding and within a spherical coherent precipitate for atoms that are undersized compared to the host and the distorted region near a planar interstitial loop. The precipitate model illustrates specifically that the lattice distortions associated with an undersized, coherent, second-phase particle (such as Co in Cu [31]) correspond to a smaller (and uniform) lattice parameter inside the particle. The precipitate model shows further that the coherency strain related to the smaller precipitate volume pulls the surrounding lattice inward toward the particle and thus produces a positive strain in the surrounding host lattice.

The interstitial loop model emphasizes that interstitial loops have compressed regions (negative strain) above and below the loop plane and only small expanded regions near the dislocation line that defines the edge of the loop. Of course, vacancy loops are just the opposite; they generate an expanded region normal to the loop plane as the surrounding lattice planes relax into the vacant loop area and only a small compressed region just inside the dislocation line at the circumference of the loop. The fact that interstitial loops are extrinsic defects in which the defect atoms occupy nonlattice positions and vacancy loops are intrinsic defects in which the missing atoms are on lattice sites leads to an asymmetry between vacancy and interstitial loops [8,11]. In addition, the compressed region at the circumference is inside the dislocation line for vacancy loops and the expanded region is outside the dislocation line for interstitial loops, which leads to a slight asymmetry in the cross sections for vacancy and interstitial loops as well.

Considering first the case of dislocation loops, the local Bragg scattering interpretation [7,8,14,32] of scattering from the asymptotic region contains direct information on the vacancy/interstitial nature of loops through sensitivity to the sign of the lattice strain in the direction normal to the loops. Numerical calculations of the lattice distortions around loops in elastically anisotropic cubic crystals have shown that the loop normal displacements depend nearly linearly on r within a volume of radius R [33] and that the strain (given by the gradient of the displacements) in regions normal to the plane of edge-type loops is given by $\Delta d / d \approx -b / 4R$ for metals [14,33], where b is the magnitude of the Burgers vector of the loop, taken to be positive for interstitial and negative for vacancy loops.

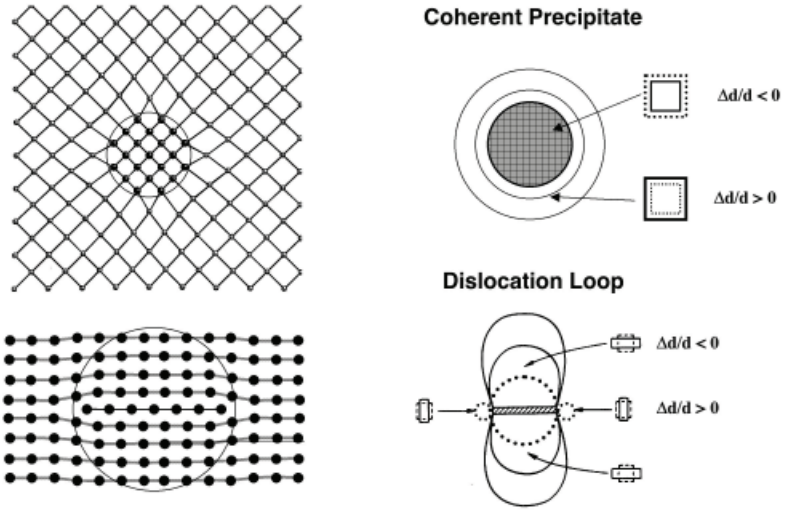

Figure 9.1. *Schematic view of the lattice distortions around coherent precipitates and interstitial loops. The precipitate lattice parameter is smaller than the host, yielding displacements that expand the surrounding lattice. The dislocation loop introduces a compressive strain normal to the loop plane in the surrounding host lattice. The circles enclose regions of nearly constant lattice parameter.*

Therefore, for loops oriented normal to H, there is a positive modulation in the ~$1/q^4$ falloff of the asymptotic scattering at the position $q = bH / 4R$, which is followed by a falloff more rapid than $1/q^4$ in the intensity for larger q values. Since it is the $1/r^2$ dependence of $\mathbf{s}(\mathbf{r})$ closer and closer to defect cluster centers that gives rise to the $1/q^4$ intensity for larger and larger q values in the asymptotic scattering region, the local Bragg scattering pileup of the intensity is due to a nearly uniform lattice parameter inside the circle containing the loop in Figure 9.1, which is caused by the displacements reaching a limiting value of $s(\mathbf{r}) = b / 2$ as r goes to zero (i.e., at the loop plane) [33].

Figure 9.2 shows numerical calculations of the diffuse scattering cross section for both vacancy and interstitial loops in Cu using Equation 9.13 [11,14,33], with lattice displacements calculated using anisotropic elasticity [33]. Since the cross sections are scaled by q^4/R^2, the lack of an extended flat region indicates the lack of an extended $1/q^4$ falloff region, and the nearly equal peak heights independent of size indicate that the scattering is proportional to the number of point defects contained in loops (i.e., loop volume = $b\pi R^2$). In this form, it is possible to see directly the departure of the scattering from an extended $1/q^4$ dependence [14] to a local Bragg scattering peak at a loop radius-dependent position of $q = bH / 4R$, as discussed above. The fact that vacancy loops scatter predominantly at negative q and interstitial loops scatter predominantly at positive q is also a direct result of the local Bragg scattering nature of the scattering, for which the compressive strain near interstitial loops puts the scattering at q higher than that of the average lattice and the expansive strain near vacancy loops puts the scattering at lower q than the average lattice Bragg position. This result is very significant for the asymptotic scattering region because the sign of b (i.e., vacancy or interstitial type) can be determined by the direction

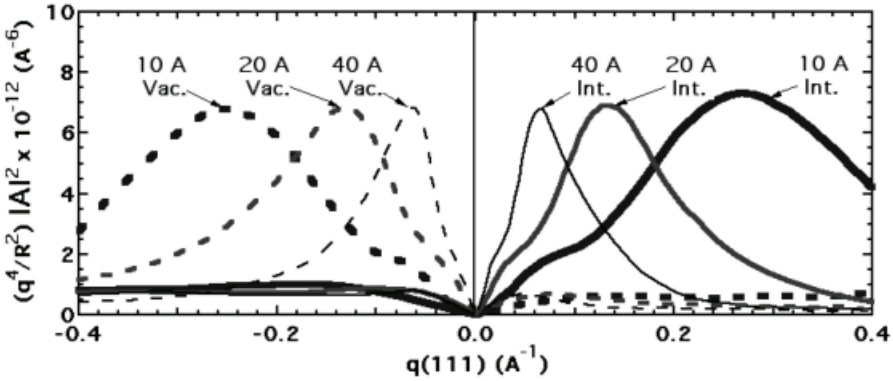

Figure 9.2. *Diffuse scattering cross sections calculated for vacancy and interstitial loops scaled by q^4/R^2 as a function of the loop radius for q values radial along the [111] direction at the (222) reciprocal lattice point for Cu.*

of q relative to H, and the radius R can be inferred from the magnitude of q. Because there are no large regions with expanded lattice parameters for interstitial loops, there is no significant scattering for negative q values associated with interstitial loops, and vice versa for vacancy loops [14].

Turning now to asymptotic diffuse scattering for coherent precipitates, one finds that different but entirely analogous local Bragg scattering effects occur. As depicted schematically in the model of a precipitate lattice at the top of Figure 9.1, the $\sim 1/r^2$ form of the distortion field terminates abruptly at the radius of the precipitate; inside the precipitate, the displacements fall linearly to zero as a direct result of the fact that coherent precipitate lattices have a (constant) lattice parameter different from the host. Of course, regions with a constant lattice parameter generate local Bragg scattering at a radial position $q = -\varepsilon H$ relative to the host Bragg position, where ε is the fractional difference between the lattice parameter of the precipitate and the host [10,12]. In contrast to the case for dislocation loops, however, the departure from $1/r^2$ for precipitates does not simply redistribute the intensity within the $1/q^4$ region. The strain of the precipitate is of the opposite sign to that generated in the host lattice, which puts the local Bragg scattering from the precipitate particle on the opposite side of the host Bragg position from the local Bragg scattering from the highly distorted region of the surrounding host lattice. These effects have long been appreciated in general [1,23,24], but they have been analyzed in more detail and discussed quantitatively in connection with numerical diffuse scattering calculations for precipitates in an isotropic elastic material by Iida et al. [10]. Figure 9.3 shows diffuse scattering cross section calculations for the (400) reciprocal lattice point for 25, 50, and 75 Å precipitates with internal strain $\varepsilon = -1.5\%$. Scaled by q^4/R^3, the form of the cross sections appears rather similar to those in Figure 9.2 for interstitial loops. In the sense that the q^4-scaled asymptotic scattering has a single peak on the positive q side for both precipitates and interstitial loops, it is a direct indication that they are both characterized by regions with lattice parameters compressed compared to the host lattice. However, in the case of interstitial loops, the compressed region is a result of distortions in the host lattice generated by the insertion of a single extra plane of atoms and represents a local Bragg scattering pileup of the $1/q^4$ scattering due to the loss of the $1/r^2$ displacement field near the loop. In the precipitate case, the compressed lattice is the intrinsic lattice structure of the second-phase precipitate, and the $1/q^4$ scattering from the (expanded) distorted host lattice is on the opposite side of the reciprocal lattice

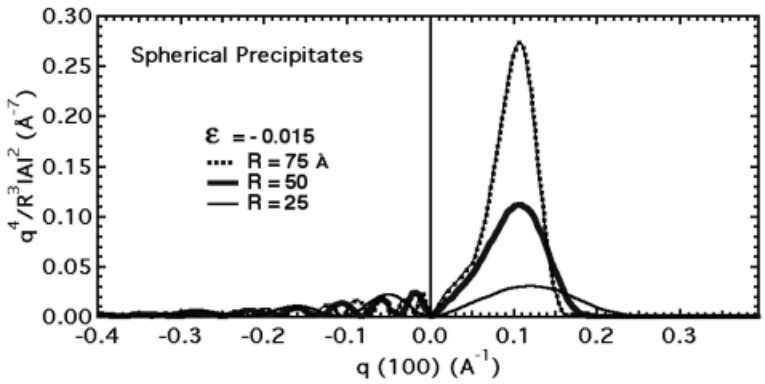

Figure 9.3. *Diffuse scattering cross section calculations scaled by q^4/R^3 for spherical precipitates with three different radii and a strain of $\varepsilon = -0.015$; the calculations were made for q along the [100] direction at the (400) reciprocal lattice point for isotropic elasticity [9].*

point. We comment that in the infinitesimal defect approximation for asymptotic diffuse scattering [5,7,10], there is no direct scattering from the defect cluster itself, and only a smooth $1/q^{10/3}$ falloff is predicted. Although this is a major shortcoming of the infinitesimal defect approximation in terms of analyzing experimental measurements, the physical insight provided by the model is very useful.

We note that in both the precipitate and dislocation loop cases, diffuse scattering radial along H contains local Bragg scattering with particle size-broadened shapes in the sense that larger clusters have smaller widths in q. The correspondence between particle size and the peak width can be only approximate, of course, because the diffuse scattering distribution is not solely Bragg scattering. In the second-phase particle case, the position of the peak, the width of the peak, the strength of the peak, and the frequency of the oscillations on the opposite side of the Bragg position all provide important information on the size and the lattice parameter of the particle, and hence on the strength of the distortions. For dislocations, the position and the width of the q^4-scaled asymptotic scattering peak provide whatever information is available on the loop size and the vacancy/interstitial nature of the loops, since the scattering on the opposite side of the periodic lattice Bragg position is relatively weak and unstructured due to the lack of significant volumes with strains of the opposite sign for loops.

5 Asymptotic Diffuse Scattering Measurements

The thrust of this chapter is to present an overview of the underlying formalism and the measurement and analysis techniques associated with X-ray diffuse scattering investigations of clustered defects. Accordingly, the remainder of the presentation focuses on selected examples of asymptotic diffuse scattering measurements and analyses for the cases of coherent precipitates and dislocation loops. A review of asymptotic (or Stokes-Wilson) diffuse scattering applications is not attempted; rather, illustrative examples of measurements performed radially along H will be selected.

Figure 9.4 shows diffuse scattering measurements made near the (400) reflection using 1.39 Å X-rays at the Cu absorption edge (to minimize Cu scattering compared to Co) on Cu(1%)Co single

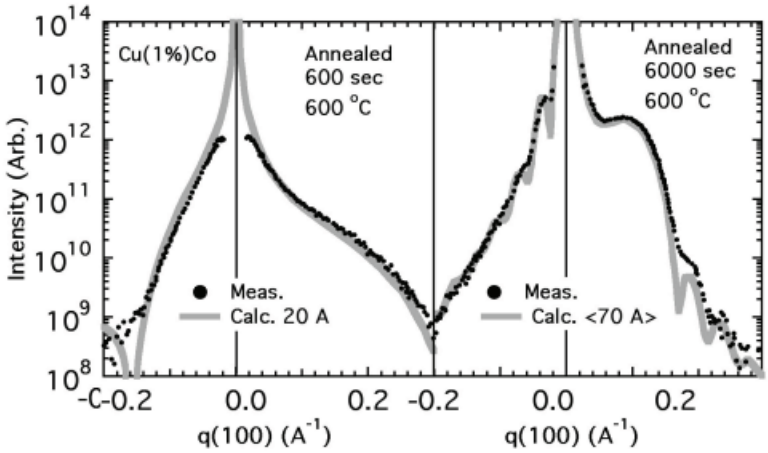

Figure 9.4. *Diffuse scattering measurements (dots) made for the wavelength of the Cu K-edge at the [400] reflection of Cu(1%)Co crystals after aging for 600 and 6000 seconds at 600 C to grow spherical coherent Co precipitates. The thick gray lines represent diffuse scattering calculations made using ε = –0.014 for 20 Å (left) and a combination of 65, 70, and 75 Å radius precipitates (weighted to contain equal volumes for each radius) in the right panel.*

crystals after thermal aging at 600 C for 600 seconds and 6000 seconds. Cu-Co is a prototype system known to form coherent spherical precipitates that increase in size by a ripening process that has been the subject of extensive investigation [35], including both X-ray diffuse scattering and small-angle neutron diffuse scattering [12,34] on a similar sample annealed for 61200 seconds at 570 C. Figure 9.6 shows diffuse scattering profiles for samples annealed for 600 and 6000 seconds compared with anisotropic elasticity calculations [12] based on face-centered cubic Co precipitates with ε = –1.4% for 20 Å radius precipitates and for an average <*R*> of 70 Å (i.e., weighted for equal volumes of 65, 70, and 75 Å precipitates) for the short and long anneals, respectively. Although the cross section calculations in Figure 9.4 do not represent fits to the measured intensities, they show that by using accurate, numerically determined scattering cross sections, remarkable agreement with measured diffuse scattering profiles can be achieved.

Figure 9.5 shows a plot of these Cu(1%)Co measurements scaled by q^4 to emphasize experimentally the fact established by the cross section calculations in Figure 9.3 that the local Bragg scattering from the precipitate particles themselves dominates the scattering in the asymptotic diffuse scattering region. The plots in Figures 9.3 and 9.5 show that scaling diffuse scattering measurements from clustered defects by q^4 provides a natural weighting for performing least-squares fitting analyses to extract defect cluster size distributions from the scattering. With the q^4 scaling, the parabolic form of the Huang scattering (which is often distorted either by imperfect/mosaic host crystals or by the lack of sufficient detector resolution both perpendicular to and in the scattering plane) that does not contain direct size information is present but not heavily weighted, while the Laue scattering containing direct size and strain information is enhanced. Results of small-angle scattering, as well as asymptotic diffuse scattering, and also references to other types of investigations of size distributions for this system are discussed elsewhere [12,31,34,35] and will not be discussed further here except to emphasize that the

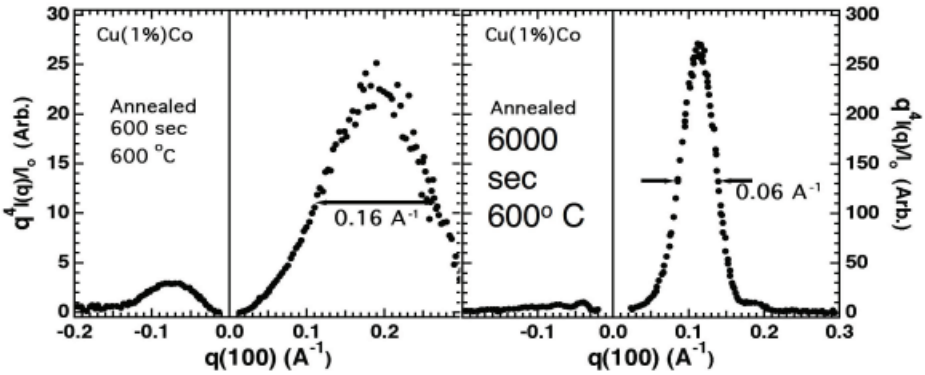

Figure 9.5. *Plots of the diffuse scattering measurements in Figure 9.4 scaled by q^4. The arrows indicate the full width at half maximum of the positive-q peaks, which are dominated by the direct (or Laue) scattering from the precipitates.*

size-dependent scaling of the intensities makes it important to obtain high-precision data and to use accurate cross sections when detailed information is desired for both large and small sizes.

The above measurement and analysis considerations hold in general for dislocation loops and other types of clustered defects as well as for coherent precipitates. Accordingly, Figure 9.6 shows the results of asymptotic X-ray diffuse scattering investigations of high-energy ion irradiation-induced dislocation loops in a Cu single crystal [14,32]. Diffuse scattering intensities measured in symmetric Bragg geometry along the [111] direction near the (222) Bragg reflection are shown scaled by q^4 out to q valu`es of 0.3 Å^{-1}. In contrast with the form of the scattering from coherent precipitates (Figure 9.5 above), we note that the q^4 scaled diffuse scattering intensity is of comparable magnitude for negative and positive q. This is, of course, due to the fact that displacement damage produces both vacancy and interstitial defects, and, as is well known, distributions of both vacancy and interstitial loops are formed in room-temperature irradiations. As discussed in connection with the loop cross section calculations in Figure 9.2, it is possible to determine qualitatively just from the positions of the peaks in the scattering that the interstitial loops have larger radii because they peak at a smaller q value. It is further possible to surmise that the total number of vacancies and interstitials condensed into loops in their respective size distributions is approximately equal, judging by the nearly equal intensities for positive and negative q, again as discussed in connection with Figure 9.2 above. While we only referenced detailed size distribution analyses for Co precipitates in Cu(1%)Co [12,34], it is of interest with respect to the nonuniform depth distribution for ion irradiated materials to discuss methods for determining absolute cluster concentrations as well as their sizes.

As is well known [14], diffuse scattering measurements made in the symmetric Bragg geometry in samples with uniform distributions of defects are related quantitatively to the scattering cross sections for a distribution of defect cluster sizes through

$$I(\mathbf{K}) = \frac{I_o}{2}{}_o \sum_i c_i(R_i) \frac{d\sigma_i(\mathbf{K}, R_i)}{d\Omega}(\Delta\Omega) \quad , \tag{9.15}$$

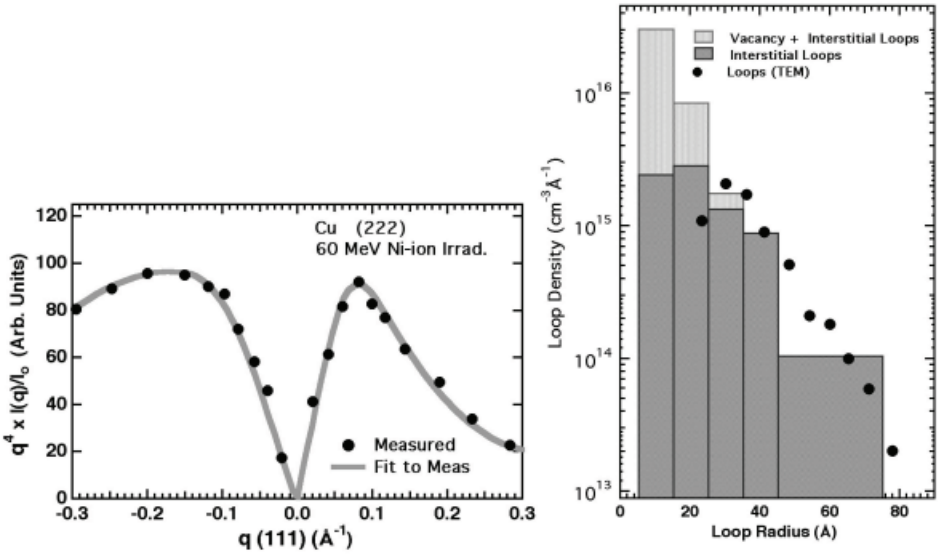

Figure 9.6. *Diffuse scattering measurements (scaled by q^4) made at the (222) reciprocal lattice point along the [111] direction for Cu irradiated with 1.3×10^{13} Ni-ion per cm^2 (left). The solid line represents a fit to the measurements with the concentrations of 10, 20, 30, 40, and 60 Å radius loops as parameters. The histograms in the right panel show the concentrations of vacancy plus interstitial loops (light shade) and the concentrations of interstitials only (dark shade). In addition, TEM measurements made on these samples show that nearly all of the vacancy loops were missed by the TEM measurements.*

where I_o is the incident beam power, $_o$ is the linear absorption coefficient, $c_i(R_i)$ is the volume concentration of defect clusters of radius R_i, and $\Delta\Omega$ is the solid angle subtended by the detector. For the case of ion irradiations, the defect distribution is uniform in the plane of the surface but is highly nonuniform in depth, with penetrations generally on the order of a few microns. Ion irradiation damage is strongly energy dependent and is dominated initially by electronic excitations that produce relatively small amounts of atomic displacements, but as the ion energy decreases, the displacement damage increases dramatically near the end of the range of the ions in the sample. Without the benefit of spatial depth resolution as discussed in the next section, it is possible to use damage energy calculations to model the profile of the displacement damage, from which the diffuse scattering intensity can be related to damage at particular depths under the assumption that the nature and type of damage is not a function of depth. Equation 9.15 then yields [14]

$$I(\mathbf{K}) = \frac{I_o}{\sin(\theta)} \sum_i c_i(t_o, R_i) \frac{d\sigma_i(\mathbf{K}, R_i)}{d\Omega} (\Delta\Omega) \int_0^\infty \frac{c_i(t)}{c_i(t_o)} e^{-2\ \ _o t/sin(\theta)}\, dt \qquad (9.16)$$

where t is the depth in the crystal, $c_i(t, R_i)$ is the depth dependence of the concentration of loops of radius R_i, and $c_i(t_o, R_i)$ is the concentration at the reference depth t_o of interest. Although this assumption has been shown to be reasonable for ion damage in metals (as discussed in the next section

on spatially resolved diffuse scattering using microbeams), this is not the case for self-ion irradiation of perfect crystal semiconductors.

Making use of Equation 9.16 for Cu irradiated to a dose of 1.2×10^{13} Ni/cm^2 with 60 Mev Ni ions and fitting the measurements with scattering cross sections for prismatic vacancy and interstitial loop radii of 10, 20, 30, 40, and 60 Å, the dislocation loop size distributions (for $t_o = 5.6$ m, the depth of the damage peak near the end of range of the Ni ions) shown at the right-hand side of Figure 9.6 were obtained. Since the units on the concentrations are expressed as loops/cm^2/Å, the area under the distributions provides the total number of loops. As discussed in more detail elsewhere [14], the average size of the vacancy loops is 12 Å, the average size of the interstitials is 22 Å, and the total number of defects in the form of loops is 6×10^{19} cm^{-3}, in which the number of vacancies and interstitials were found to be equal within ~6% (interstitials/vacancies = 47/53). Considering the logarithmic scale for the loop concentrations in Figure 9.6, we note that there are more interstitial loops than vacancy loops for the 30, 40, and 60 Å size bins, but there are approximately twice as many 20 Å vacancy loops as interstitial loops and ~15 times more 10 Å vacancy loops than interstitial loops. This trend is observed for irradiation-induced defects in metals in general [14] and is apparently a result of greater mobility for interstitial loops providing a mechanism for coalescence.

Finally, it is of interest to compare the TEM results in Figure 9.6 with the X-ray diffuse scattering results. Although the TEM results reported in the study by Narayan and Larson [22] are in good agreement with the X-ray results for loops 30 Å or more in radius, the TEM study reported no loops below a 20 Å radius. Although it is known that electron microscopy techniques are capable of imaging dislocation loops down to ~5 Å radius, it seems clear that the TEM size distribution is not complete, even at 20 Å in this case. It is possible that this is due to nonideal sample imaging conditions in the preparation of cross section samples, vacancies not fully collapsed into loops (i.e., stacking-fault tetrahedral), or a preferential loss of small loops to the surface of the thin foil sample. As discussed previously, in cases where TEM measurements separated the vacancy and interstitial loop components, it is not unusual to find a sizeable imbalance in the total vacancy and interstitial in dislocation loops [15]. The X-ray measurements in Figure 9.6 do not prove that the vacancy component is in dislocation loop form, but they do demonstrate that the vacancy component is present in the form of collapsed clusters with net distortion fields similar to vacancy loops. As mentioned above, separating the size distributions of vacancy and interstitial loops is tedious using TEM, and this is one area in particular in which asymptotic diffuse scattering represents a very attractive tool. This will be an important attribute in the spatially resolved diffuse scattering measurements of Si-ion-implanted Si, to be discussed below.

6 Spatially Resolved Diffuse Scattering Measurements on High-Energy, Self-Ion-Implanted Silicon

In the diffuse scattering techniques and examples discussed above, the incident X-ray beams were of the order of millimeters in size, so spatial resolution was not a consideration. In this closing section, we discuss spatially resolved diffuse scattering measurements of vacancy- and interstitial-type defect clusters as a function of depth dependence in high-dose self-ion-implanted Si single crystals. This system is of interest technologically in connection with the so-called vacancy implanter effect observed in high-energy ion implantation processing of electronic devices [36]. The underlying science is integrally connected with a fundamental understanding of energetic particle displacement of atoms in crystalline materials and the subsequent evolution and interactions of the displaced atoms.

Figure 9.7 shows a schematic of the scattering geometry for depth-resolved diffuse scattering measurements using X-rays focused to 0.7 m by a Fresnel zone plate [37] on the XOR/UNI ID33 beamline at the Advanced Photon Source. This cross section geometry makes possible depth-dependent measurements of defect clusters in Si irradiated with 9×10^{16} 10 MeV Si ions at a temperature of 300 C. By cleaving the implanted Si normal to the implanted surface, diffuse scattering measurements were made as a function of depth at the (220) reflection with a monochromatic X-ray microbeam [27] by translating the crystal along the [001] surface normal direction. In this cross section geometry, used recently for depth-resolved measurements of strain in MoN coatings on Si [38], not only is it possible to make submicron-resolution depth-resolved measurements on the defect distributions, but also the scattering intensity comes from sample volumes that are ~10–100 m along the beam, which enhances the defect scattering intensity significantly (~10–100 times) depending on the photoelectric absorption length. In plan-view geometry, where the incident beam is directed into the surface, submicron-resolution measurements would collect diffuse scattering from only submicron lengths along the beam.

Figure 9.8 shows a crystal translation scan monitoring the total diffuse scattering at $q = 0.04$ Å^{-1} in the [220] direction as a function of depth for the implanted Si crystal. A weak plateau of diffuse scattering is present in the first two to three microns below the surface. The plateau is followed by an order of magnitude higher peak in the diffuse scattering centered at a depth of 4.25 m, which corresponds to the end of range of the implanted silicon ions. TEM measurements [39] readily identify a dense band (0.3–0.4 m thickness) of interstitial clusters at the implanted ion end of range, but they do not see the vacancy clusters that, from indirect measurements [31], are believed to be present near the surface. It is understood that the implanted ions constitute an excess supply of interstitial atoms that do not have corresponding vacancies with which to annihilate. In addition, there is strong evidence that the forward momentum of the interstitials (as they are created by the impinging implanted ions), combined with an increasing damage density with depth, leads to a local imbalance in the number of vacancies and interstitials in favor of vacancies near the surface. Because vacancy-rich regions give rise to strongly enhanced thermal diffusion, these issues are critical for device manufacturing considerations; unfortunately, they have been difficult to understand quantitatively because of the difficulty of identifying directly the presence of vacancy clusters.

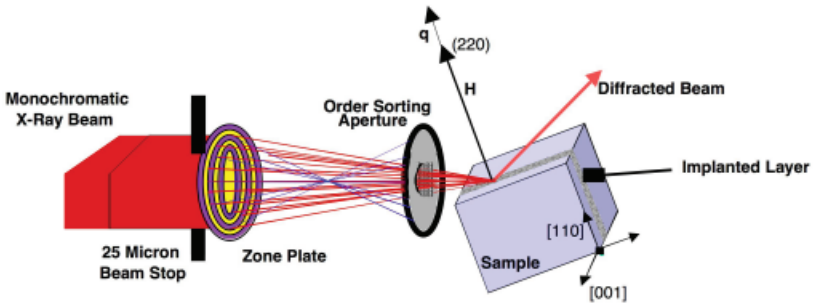

Figure 9.7. *Microbeam diffuse scattering geometry showing the Fresnel zone plate focusing element, a wire central beamstop, an aperture to limit third-order and higher order focused X-rays, and the implanted sample orientation and scattering geometry.*

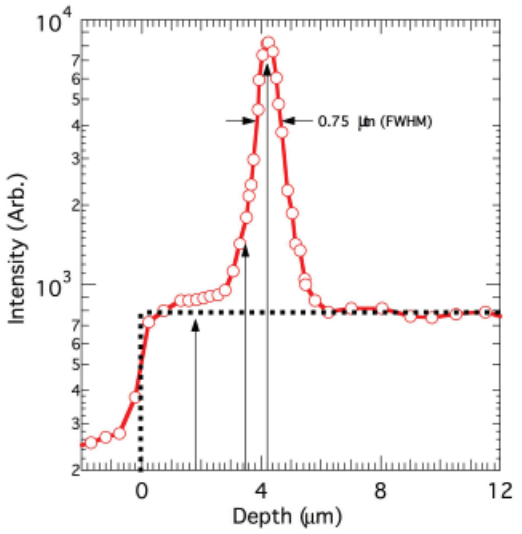

Figure 9.8. *Depth translation scan of the diffuse scattering at q = 0.04 Å^{-1} for 10 MeV self-ion-implanted silicon. The dashed lines indicate the sample edge at the defect-free silicon scattering level.*

The three vertical arrows in Figure 9.8 indicate depth positions at which the diffuse scattering measurements plotted in Figure 9.9 were performed. The scattering intensity located at d = 4.25 m strongly dominates the scattering for the range of q values measured. It can be inferred qualitatively from the diffuse scattering curves in Figure 9.9 that the defect clusters located at 4.25 m (the end of range of the implanted Si) are predominantly of the interstitial type because the much stronger intensity on the positive q side corresponds to interstitial loops. On the other hand, the relatively weaker diffuse scattering intensities at d = 3.45 and 1.80 m have more nearly equal intensities for positive and negative q, indicating the presence of an equal or larger fraction of vacancy-type loops for these depths. Analyzing the data quantitatively, the solid lines in Figure 9.9 represent least-squares fits to the measured data for vacancy and interstitial loops with radii 3.8, 11.5, 19.2, 26.9, 34.6, 42.2, and 49.9 Å; these radii correspond to integer numbers of silicon unit cells for {111} loops. To limit the number of free parameters, the concentrations in Equation 9.16 for R = 26.9 and 34.6 Å were constrained to have the same number of point defects and similarly for R = 42.2 and 49.9 Å.

The size distributions corresponding to the solid line fits in Figure 9.9 are plotted in Figure 9.10. The results are presented in the form of histograms of the relative concentrations of vacancy and interstitial loops centered at the radii of the cross section calculations. Also included in Figure 9.10 are values for the relative number of point defects, N'_{PD}, contained in the loop distributions. The quantitative fits to the diffuse scattering are consistent with the (above) qualitative interpretation of the data in the sense that the number of interstitial loops in the distribution (and the number of point defects in the interstitial loops) is overwhelmingly larger than the number for vacancies at d = 4.25 m. This is consistent with the expected oversupply of interstitials in this region due to the end of range of the implanted Si ions. At d = 1.80 m, on the other hand, the number of vacancy loops and the total number of vacancies stored in loops is larger than the corresponding number for interstitials.

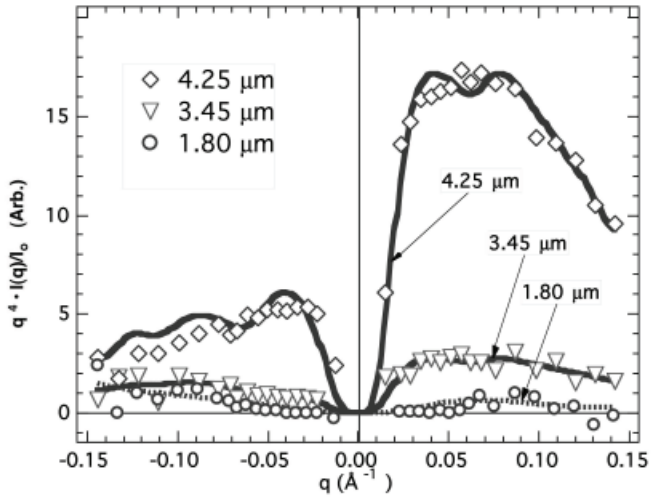

Figure 9.9. *Depth-resolved diffuse scattering weighted by q^4. Measurements as a function of q were performed at three depths identified by arrows in Figure 9.8. The solid lines represent least-squares fitting of the measured data to determine size distributions of vacancy and interstitial loops.*

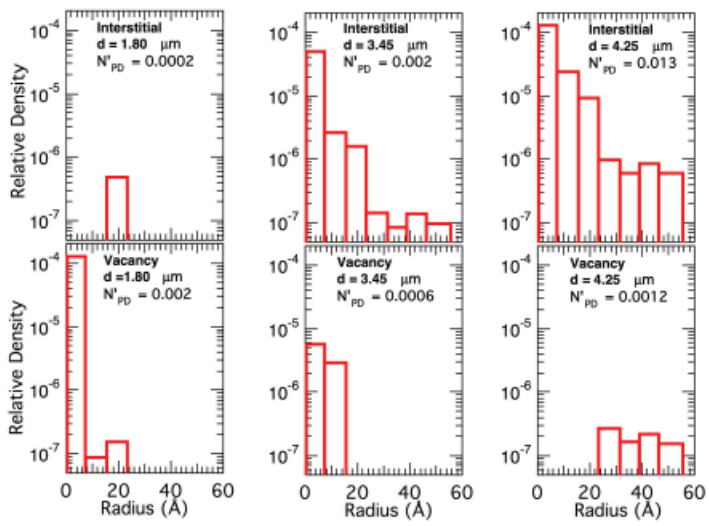

Figure 9.10. *Vacancy and interstitial loop size distributions corresponding to the three measurements in Figure 9.9. Relative concentrations of point defects N'_{PD} contained within the loop distributions are provided.*

Of course, the results for the 1.80 m position are less reliable than for the other two positions measured because of the low intensities, indicating the need for additional measurements. Nevertheless, within the measurement uncertainty in the 1.80 m measurements, we note that the vacancy components for both d = 3.45 and 1.80 m trend toward a higher ratio of vacancies to interstitials and that the number of interstitials is lowest near the surface, both of which are consistent with expectations for this region. Considering the extremely high defect density in the narrow (~0.3–0.4 m) defect band observed by electron microscopy [39], it is likely that the interstitial component at d = 3.45 m contains a nonnegligible contribution from the tail of the spatial resolution of the microbeam; however, the measurements for d = 1.80 m should not be significantly impacted by the tails of the spatial resolution even though the scattering intensities are quite low.

Although these depth-resolved diffuse scattering results are in need of improved statistical precision in the measurements as well as higher spatial resolution, they suggest new directions for diffuse scattering investigations as microbeam capabilities develop, and the results demonstrate the potential for new information from depth-resolved studies of ion implantation-induced defects in particular. Just as with spatially integrated measurements, spatially resolved X-ray diffuse scattering measurements are complementary to electron microscopy measurements in their sensitivity to small defect clusters, and they provide a method for direct separation of the vacancy and interstitial components that has been difficult for TEM at small sizes.

7 Summary and Concluding Remarks

The underlying formalism that has been developed for diffuse scattering generated by lattice defects in crystalline materials provides both a physical understanding of the origin of diffuse scattering from clustered defects and a sound basis for quantitative analyses of experimental measurements in terms of the type, size, and concentration of defect clusters. The Huang scattering close to Bragg reflections provides direct information on the local defect symmetry through the sensitivity of the Huang scattering to the form of the long-range elastic distortions. On the other hand, the asymptotic diffuse scattering at somewhat larger distances q from reciprocal lattice points provides a local Bragg-scattering mapping of the highly deformed lattice in the immediate neighborhood of defect clusters.

When analyzed using accurate, numerically calculated scattering cross sections based on actual deformation fields for both large and small distances from defect clusters, it is possible to extract detailed information on the size distributions and concentrations of defect clusters. The sensitivity of local Bragg-like scattering to the sign of the elastic strain (i.e., $\pm$ strain $\rightarrow \mp q$) provides intuitive insight into the presence of vacancy or interstitial loops, and similarly, into the presence of coherent precipitates with undersized/oversized lattices with respect to the host lattice. Moreover, the magnitude of the distorted lattice strains and particle-size broadening combine to provide remarkable sensitivity to cluster sizes. The R^2 and R^3 weighting of asymptotic diffuse scattering cross sections for dislocation loops and coherent precipitates, respectively, conveniently renders the overall scattering sensitive to the total number of point defects contained in the size distribution. However, this weighting of the asymptotic scattering and the fact that the Huang scattering is weighted by the fourth and sixth powers of R necessitates the use of both highly accurate cross sections and accurate diffuse scattering measurements over the entire q range in order to extract reliable size distributions. This is particularly important for broad size distributions with widely varying sizes and for bimodal size distributions with disparate sizes.

Accurate characterization of defect cluster distributions should, in principle, be made using diffuse scattering distributions from measurements around a number of different types and orders of reciprocal lattice positions. Although comprehensive measurements of full three-dimensional volumes in q space are now feasible with modern synchrotron X-ray sources and high-resolution X-ray area detectors, such measurements and detailed analyses of the resulting measurements for clustered defects do not seem to be made in present practice. In lieu of comprehensive measurements to constrain fits and analyses, combinations of TEM measurements and X-ray diffuse scattering measurements can be exploited to reduce ambiguities and increase the accuracy of diffuse scattering results. In particular, when more than one type of defect cluster are either present or potentially present, TEM measurements can provide valuable information within their resolution limits. Conversely, for small cluster sizes and defect distributions containing both vacancy and interstitial loops, diffuse scattering measurements can often provide information on the sizes below the resolution limit for TEM investigations of clustered defects.

As discussed in the previous section, the availability of submicrometer-diameter X-ray beams at synchrotron sources now provides the possibility of spatially resolved diffuse scattering measurements. The spatial resolution of X-ray microbeams or nanobeams will remain complementary to electron microscopy in view of the sub-Ångstrom spatial resolution capability of new high-resolution electron microscopy systems; however, TEM sample sectioning techniques are inherently destructive of the sample environment. Moreover, there are entire classes of materials issues associated with the so-called mesoscale regime (approximately tenths of microns to hundreds of microns) for which spatial resolution of a few Ångstroms is not required, but nondestructive investigations with submicron spatial resolution over, say, tens of microns are needed; grain sizes of structural materials are often in the range of a few microns to tens of microns, for instance.

The example discussed above of 10 MeV self-ion-implanted Si is the type of case in which the sample-sectioning process for TEM may have led to the dissolution or surface escape of small vacancy clusters; nondestructive microbeam techniques preserve the bulk nature of the sample associated with the implantation. There are, of course, issues to deal with in terms of microbeam or nanobeam X-ray investigations that perhaps have not been adequately addressed at this point. For instance, the assumption of a statistically large number of defects/clusters within the diffracting volumes may not be fulfilled for precipitates of large size and sparse density, and the impact of edge effects associated with diffraction from beams with submicron to a few nanometers beams have not been carefully addressed up to now. In general, detailed experimental and theoretical investigations definitively testing the limits of even nonspatially resolved diffuse scattering techniques would be useful; most investigations appearing in the literature understandably focus on the perceived successes of diffuse scattering measurements, and convincing demonstrations of the limits of applicability are difficult to find in the literature.

Establishing definitive limits for diffuse scattering from statistical distributions does not necessarily define limitations of X-ray scattering investigations; rather, they tend to point to entirely new opportunities, such as the transition to the regime of imaging individual lattice defects rather than entire ensembles of defect clusters for larger defect aggregates that often occur in low densities, for instance. Moreover, forward-direction [40] and high-angle [41] coherent diffraction direct Fourier inversion X-ray techniques are being developed that offer the possibility of three-dimensional imaging with resolution from a few nanometers down to atomic resolution. To be sure, direct inversion imaging (i.e., so-called lensless imaging) is at present not close to atomic resolution, nor is it even imminent for X-rays because significant increases in beam brilliance are needed. However, the brilliance of new

and planned synchrotrons continues to increase, and there are no fundamental limitations precluding such resolutions [42] using large numerical aperture X-ray geometries associated with high-angle diffraction. After all, crystallography techniques involving (large-angle) Bragg reflections have provided atomic resolution information on periodic structures for nearly a century.

Acknowledgments

The author acknowledges the vital contributions of collaborators J. Barhorst, J. Chung, P. Ehrhart, M. Galloway, T. Haynes, G. Ice, S. Iida, R. Kalayanaraman, J. Lewis, S. Ohr (deceased), W. Schmatz (deceased), S. Spooner, J. Tischler, H. Trinkaus, M. Yoon, F. Young Jr. (deceased), W. Yun, and P. Zschack in the diffuse scattering investigations discussed in this chapter, and A. Meldrum and V. Venezia are thanked for access to TEM measurements. Oak Ridge National Laboratory (ORNL) research was sponsored by the U.S. Department of Energy (DOE), Basic Energy Sciences Division of Materials Sciences and Engineering. The Advanced Photon Source and the National Synchrotron Light Source are supported by the DOE Office of Science.

References

1. M. A. Krivoglaz, *Theory of X-ray and Neutron Scattering by Real Crystals* (New York: Plenum Press, 1969).
2. P. H. Dederichs, *Phys. Rev. B* 1 (1970): 1306.
3. P. H. Dederichs, *Phys. Rev. B* 4 (1971): 1041.
4. H. Trinkaus, *Phys. Stat. Sol.* 54 (1972): 209.
5. P. H. Dederichs, *J. Phys. F: Met. Phys.* 3 (1973): 471.
6. H. Trinkaus, *Phys. Stat. Sol. (b)* 51 (1972): 307.
7. H. Trinkaus, *Z. Angew. Phys.* 31 (1971): 229.
8. P. Ehrhart, H. Trinkaus, and B. C. Larson, *Phys. Rev. B* 25 (1982): 834.
9. S. M. Ohr, *J. Appl. Phys.* 43 (1972): 1361.
10. S. Iida and B. C. Larson, *J. Mater. Res.* 3 (1988): 267.
11. B. C. Larson and W. Schmatz, *Phys. Stat. Sol. (b)* 99 (1980): 267.
12. B. C. Larson, S. Iida, J. Z. Tischler, J. D. Lewis, G. E. Ice, and A. Habenschuss, *Characterization of Defects in Materials*, ed. R. W. Siegel, R. Sinclair, and J. R. Weertman, vol. 82 (Pittsburgh: Materials Research Society, 1987), 73.
13. P. Ehrhart, and R. S. Averback, *Phil. Mag. A* 60 (1989): 283.
14. B. C. Larson and F. W. Young, *Phys. Stat. Sol. (a)* 104 (1987): 273.
15. B. C. Larson and J. F. Barhorst, *Defects in Semiconductors*, ed. J. Narayan and T. Y. Tan (Amsterdam: North Holland, 1981), 151.
16. P. Ehrhart, *J. Nuc. Mat.* 216 (1994): 170.
17. P. H. Dederichs, *Solid State Physics* 27 (1972): 135.
18. B. C. Larson, *J. Appl. Cryst.* 8 (1975): 150.
19. H. Peisl, *J. Appl. Cryst.* 8 (1975): 143.
20. K. Nordlund, P. Partyka, R. S. Averback, and I. K. Robinson, *J. Appl. Phys.* 88 (2000): 2278.
21. Y. Zhong, Y. Bailat, R. S. Averback, S. K. Ghose, and I. K. Robinson, *J. Appl. Phys.* 96 (2004): 1328.
22. J. Narayan, and B. C. Larson, *J. Appl. Phys.* 48 (1977): 4536.
23. M. A. Krivoglaz, *Phys. Met. Metall.* 9 (1960): 641.
24. M. A. Krivoglaz and K. P. Ryaboshapka, *Phys. Met. Metall.* 16 (1963): 641.
25. A. P. Shpak, V. B. Molodkin, S. I. Olikhovskii, Y. M. Kyslovskyy, O. V. Reshetnyk, T. P. Vladimirova, E. G. Len, A. I. Nizkova, V. M. Venger, and S. V. Dmitriev, *Phys. Stat. Sol. (a)* 204 (2007): 2651.
26. R. I. Barabash and M. A. Krivoglaz, *Phys. Met. Metall.* 45 (1978): 1.

27. M. Yoon, , B. C. Larson, . J. Z. Tischler, T. E. Haynes, J.-S. Chung, G. E. Ice, and P. Zschack, *Appl. Phys. Lett.* 75 (1999): 2791.
28. A. R. Stokes and A. J. C. Wilson, *Proc. Phys. Soc.* 56 (1944): 174.
29. M. Lax, *Rev. Mod. Phys.* 23 (1951): 287.
30. P. Ehrhart and W. Schilling, *Phys. Rev. B* 8 (1973): 2604.
31. B. C. Larson and W. Schmatz, *Phys. Rev. B* 10 (1974): 2307.
32. B. C. Larson and F. W. Young Jr., *Point Defects and Defect Interactions in Metals*, ed. J. Takamura, M. Doyama, and M. Kiritani (Tokyo: University of Tokyo Press, 1982), 679.
33. S. M. Ohr, *Phys. Stat. Sol. (b)* 64 (1974): 317.
34. S. Spooner, S. Iida, and B. C. Larson, *Characterization of Defects in Materials*, ed. R. W. Siegel, R. Sinclair, and J. R. Weertman, vol. 82 (Pittsburgh: Materials Research Society, 1987), 79.
35. W. Wagner, J. Piller, H.-P. Degischer, and H. Wollenberger, *Zeitschrift für Metallkunde* 76 (1985): 693.
36. R. Kalayanaraman, T. E. Haynes, O. W. Holland, H.-J. L. Gossmann, C. S. Rafferty, and G. H. Gilmer, *Appl. Phys. Lett.* 79 (2001): 1983.
37. B. Lai, W.-B. Yun, D. Legnini, Y. Xiao, J. Chrzas, P. J. Viccaro, V. White, S. Bajikar, D. Denton, F. Cerrina, E. Di Fabrizio, M. Gentili, L. Grella, and M. Baciocchi, *Appl. Phys. Lett.* 61 (1992): 1877.
38. G. Chen, D. Singh, O. Eryilmaz, J. Routbort, B. C. Larson, and W. Liu, *Appl. Phys. Lett.* 89 (2006): 172104.
39. V. C. Venezia and A. Meldrum, private communication (2000).
40. J. Miao, T. Ishikawa, E. H. Anderson, and K. O. Hodgson, *Phys. Rev. B* 67 (2003): 174104.
41. I. A. Vartanyants, I. K. Robinson, I. McNulty, C. David, P. Wochner, and T. Tschentscher, *J. Synchrotron Rad.* 14, 453. (2007).
42. B. C. Larson and B. Lengeler, *MRS Bulletin* 29 (2004): 152.